IEEE Access
Multidisciplinary | Rapid Review | Open Access Journal

Received May 31, 2019, accepted June 14, 2019, date of publication June 20, 2019, date of current version July 8, 2019.

Digital Object Identifier 10.1109/ACCESS.2019.2923990

Preamble Design for UAV Communications Over Cellular Networks

SU HYUK MOON[1], CHANG HWAN PARK[2], AND YONG SOO CHO[1]
[1]Department of Electrical and Electronics Engineering, Chung-Ang University, Seoul 06794, South Korea
[2]LG Electronics, Seoul 06772, South Korea

Corresponding author: Yong Soo Cho (yscho@cau.ac.kr)

This work was supported by the National Research Foundation of Korea (NRF) grant funded by the Korean Government (MSIT) under Grant 2018R1A4A1023826.

ABSTRACT Unmanned aerial vehicle (UAV) communications over cellular networks are currently gaining increased interest because it can enable real-time control of UAVs and wide-area coverage. We discuss various challenges for future UAV cellular networks, where cellular networks with down-tilted antennas optimized for terrestrial users can extend terrestrial cellular services to aerial users. To overcome challenges such as large channel variation and UAV power consumption in UAV cellular networks, we propose a technique of preamble design for these networks using scalable sequences. Specifically, three types of scalable sequences are proposed for efficient use of battery power in UAVs, namely, maximum-length scalable sequence, Zadoff–Chu scalable sequence, and linear frequency modulated (LFM) scalable sequence. The properties of these scalable sequences are analyzed and compared through simulations in different channel environments.

INDEX TERMS Cellular network, preamble design, scalable sequence, unmanned aerial vehicle.

I. INTRODUCTION

With high mobility and low cost, unmanned aerial vehicles (UAVs), commonly known as drones, are attracting increased interest because of their wide range of applications. Although UAVs have been developed as military technology to reduce pilot losses in hostile territories, commercial UAVs are being rapidly adopted in several areas, including remote sensing, delivery, surveillance, search and rescue, aerial photography, agriculture, and communication relaying [1]–[8].

Two different types of control schemes have been mainly used on UAVs, namely, autonomous and standalone control. In the former, a mission is accomplished using onboard computers to track predefined path information. However, real-time control is not possible with this scheme if an emergency intervention is needed. In standalone control, WiFi connectivity is normally used to remotely control UAVs in real time. However, WiFi connectivity may be lost for beyond line-of-sight (LoS) communication. Thus, cellular networks have been considered for providing ubiquitous coverage by exploiting the ground infrastructures of mobile operators that offer wide-area, high-speed, and secure wireless connectivity.

The associate editor coordinating the review of this manuscript and approving it for publication was Moayad Aloqaily.

Recently, the telecommunications industry and the 3rd Generation Partnership Project (3GPP) have shown a great interest in cellular-based communication for UAVs to extend terrestrial cellular services for aerial users in the upcoming 5G networks. In March 2017, the 3GPP project defined a study item with four fundamental objectives regarding UAVs: traffic requirements, channel model, performance analysis, and communication enhancements. According to the measurement results in [9] and [10], the percentage of UAVs experiencing cell-edge conditions is much higher as compared to terrestrial user equipments (UEs). This is because UAVs, due to their high LoS propagation probability, receive downlink interference from a large number of cells than a typical terrestrial UE does. Also, with more favorable propagation conditions in the sky, UAVs may generate more uplink interference to neighbor cells while experiencing more downlink interference from those cells. In [11]–[13], interference mitigation techniques for UAVs served by cellular networks are proposed.

In order to solve the interference problem in UAV cellular networks, 3D beamforming arrays are considered to track the LoS direction between base station (BS) and UAV. In this approach, the 3D beamformer at the BS tracks the LoS direction of UAV and steers the antenna boresight towards the UAV. In [14]–[16], different 3D beamforming techniques

are proposed for UAV communication. In [17], a preamble-based beam training technique is proposed to track multiple UAVs in synchronous and asynchronous channel environments. In [18], a hybrid beamforming technique for BS-to-UAV communications is proposed based on the observation that the wider beamwidth requires less training overhead but results in lower beamforming gain. In [19], a pilot-based channel tracking technique for mmWave UAV communications is proposed by exploiting the angle reciprocity. However, in these techniques, additional 3D beamformers should be installed at the BS for UAV communication while antenna arrays at the BS in current cellular networks are used to serve terrestrial UEs.

It is also shown in the measurement results [9] that UAVs flying above the boresight of antenna arrays at the BS are likely to be served by sidelobes of the antenna array, because current cellular networks are optimized for terrestrial users. As BS antennas are down-tilted to confine the cell radius and thus mitigate inter-cell interference, the characteristics of radio links for UAVs differ from terrestrial cellular connection [20]. In fact, a UAV will receive a different signal strength depending on the altitude because the received signal strength (pathloss) varies depending on sidelobe patterns [21]. In addition, when the UAV does not receive a signal due to the presence of a null between sidelobes, it may be served by a distant BS (with different cell ID) instead of a geographically close BS. In this case, the pathloss will increase due to the long distance [22]. Consequently, the UAV will experience a large pathloss variation and require connection to other BS depending on its altitude.

Another challenge in UAV operation is the limited battery capacity. The UAV flight time is restricted to approximately 20 min, as imposed by the onboard battery capacity. Hence, new techniques for increasing flight time considering the very limited battery capacity should be developed to increase the adoption of UAVs for different applications. In [23], several approaches are discussed for a network operator to address the UAV battery lifetime issue and design a UAV network that enables continuous wireless coverage. Three battery charging options are described for UAV cellular networks. In [24], an optimization problem is formulated to minimize the energy consumption of drones in addition to determining the placement of these drones and guaranteeing a minimum rate for the users. In [25], a joint optimization technique of route planning and task assignment is proposed for UAV-aided mobile crowd sensing systems to minimize the energy consumption of UAVs.

Like terrestrial cellular systems, a UAV attempting to access a BS is required for synchronization and cell search, which are essential for successful association and connectivity to the network. Synchronization in a UAV cellular network may include symbol timing acquisition and frequency synchronization. Cell search, on the other hand, involves the estimation of a physical cell ID. Preambles are transmitted by individual BSs to facilitate the UAV acquisition of synchronization parameters and cell ID. After synchronization and cell search, the UAV will be able to demodulate command and non-payload communication (CNPC) messages. Thus, the preambles for synchronization and cell search must be robust to guarantee detection by UAVs even in high-speed environments that induce the Doppler effect [26], [27].

To address the challenges in UAV cellular networks, we propose a new preamble design technique for next-generation UAVs, using scalable sequences (SSs). The proposed SSs are generated at the BS with the full available bandwidth because there is no power constraint at the BS. On the other hand, the UAV receives the SS with different bandwidth depending on the channel condition, as the UAV will experience large pathloss variations depending on its altitude and the BS sidelobe pattern. Specifically, the signal strength received by the UAV will be weak when the pathloss between the BS and UAV is large. In this case, a full bandwidth is used in the proposed technique to increase the detection probability of synchronization parameters and cell ID. When the pathloss is small, the signal strength received by the UAV will be strong. In this case, a small bandwidth is used to reduce UAV power consumption, as the synchronization parameters and cell ID can be easily detected. If a conventional preamble is used in this case, some synchronization parameters or the cell ID may not be detected due to bandwidth mismatch (waveform mismatch). In contrast, the proposed SS is designed to provide the correct synchronization parameters and cell ID even under different bandwidths at the receiver (i.e., UAV). Overall, the SS enables UAVs to increase detection performance using a large bandwidth under poor channel conditions and reduce battery consumption using a small bandwidth under good channel conditions.

The rest of paper is organized as follows. In section II, the concept of SS is introduced for UAV cellular networks. Three different types of SSs are proposed for efficient use of the UAV battery capacity, namely, maximum-length SS (M-SS) in section III, Zadoff–Chu SS (ZC-SS) in section IV, and linear frequency modulated SS (LFM-SS) in section V. The properties of these SSs are analyzed and verified through simulations in these sections. In section VI, the performance of the SSs are compared through simulations in different channel environments. Finally, conclusions are drawn in section VII.

II. SS DESIGN

Fig. 1 shows a typical scenario of UAV communications over cellular networks. The BS in a cellular network normally has down-tilted antennas to reduce co-channel interference and confine the cell coverage area. Flying UAVs are likely to be served by the sidelobes of BS antennas. Consequently, the UAVs will receive varying signal strength depending on their altitude by the sidelobe patterns of BS antennas. The UAV may receive a relatively strong signal if aligned with the sidelobe direction, and no signal if located over a sidelobe null. In the latter case, the UAV may be served by a neighboring BS after making a handover. Thus, the UAV will experience a large variation of the channel characteristic

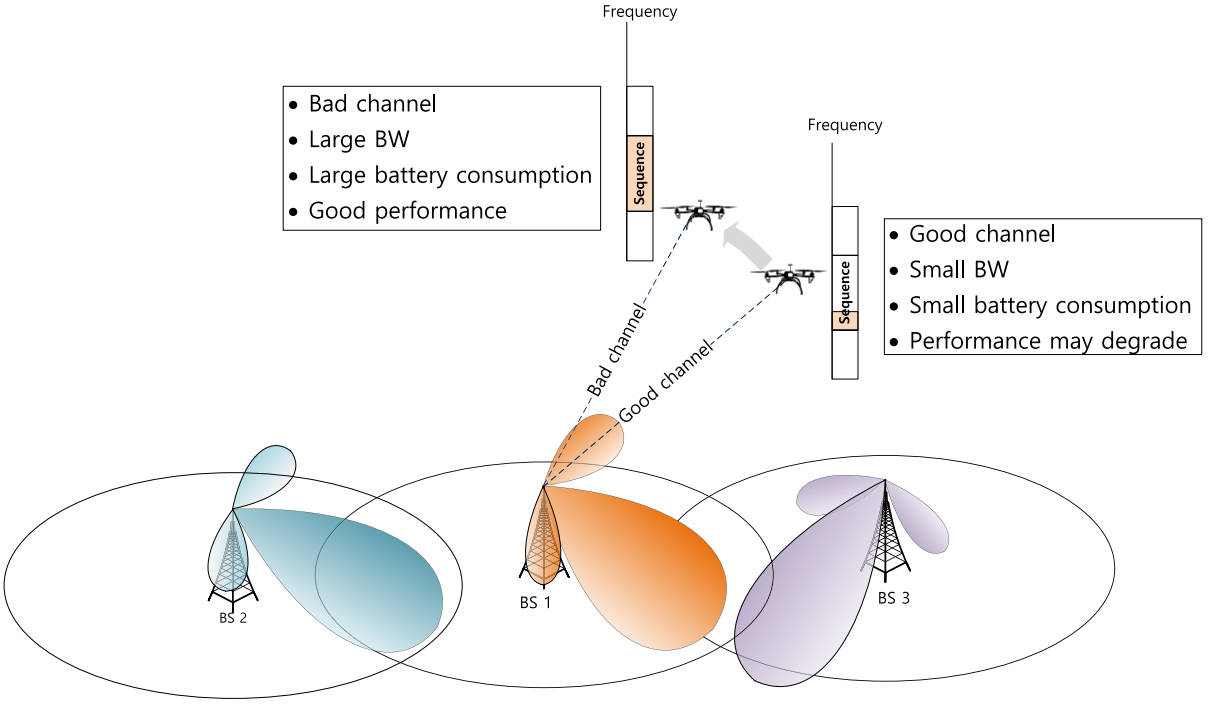

FIGURE 1. Typical scenario of UAV communications over cellular networks.

(i.e., pathloss) and switch among different BSs depending on its altitude.

We devise a new preamble design technique for UAV cellular networks to efficiently use the UAV battery capacity in a channel environment with down-tilted antennas. In the proposed technique, the preamble is generated at the BS with full length N and transmitted using all the available bandwidth, given the lack of power constraints in the BS. The UAV receives the preamble with bandwidth according to the channel condition. When the UAV receives a weak signal, it detects the preamble using the full bandwidth. In this case, full-length N preamble sequence is used to increase the detection probability of synchronization parameters and cell ID. When the UAV receives a strong signal, it detects the preamble using a small bandwidth. In this case, a portion L ($L < N$) of the preamble sequence is used as reference signal at the UAV to reduce power consumption because there is no difficulty in detecting synchronization parameters and cell ID.

In general, the UAV energy consumption is composed of two main components, namely the propulsion energy and communication related energy [28], [29]. To reduce communication energy, we should use a smaller bandwidth because the energy consumption is linearly proportional to bandwidth. Note that the total energy of a time domain signal is the same as the energy of the corresponding frequency domain signal (Parseval's theorem). As the UAV receives a signal with larger bandwidth, its communication energy consumption increases.

In this paper, the concept of the SS is proposed to efficiently use the UAV battery capacity by changing the bandwidth depending on the channel condition. We define the SS as a sequence that preserves information (i.e., synchronization parameters and cell ID) even with a portion of the sequence in the receiver. In general, information cannot be preserved at the receiver if the preamble is acquired at a narrower bandwidth than the transmission one. However, when the SS is used to generate the preamble in UAV cellular networks, the information can be detected even at a narrow bandwidth. Fig. 2 shows a flow chart for the proposed scalable sequence design. In this paper, we only consider timing as synchronization parameter, because the carrier frequency offset can be easily estimated with a repetitive pattern in any type of preamble. In the sequel, we propose three different types of SSs for UAV cellular networks. We verify whether the SSs correctly provide the information (i.e., timing and cell ID) with a narrow bandwidth. We also discuss the required conditions for the sequences to be scalable.

III. M-SS

Maximum-length sequences (m-sequences) are used for preamble design in systems based on orthogonal frequency division multiplexing (OFDM) such as LTE and 5G new radio (NR) systems [30], [31]. As our design is also based on OFDM cellular systems, the M-SS is generated like the NR primary synchronization signal (PSS) at the transmitter. An m-sequence of length N is generated at the BS and allocated to N subcarriers in the frequency domain. Then, the time-domain sequence of length N, obtained from the inverse discrete Fourier transform (IDFT) of the m- sequence, is transmitted by the BS as a preamble. However, in M-SS, the preamble is received at the UAV with a bandwidth according to the channel condition. A bandwidth corresponding to L ($L \leq N$) subcarriers is used at the receiver (i.e., UAV)

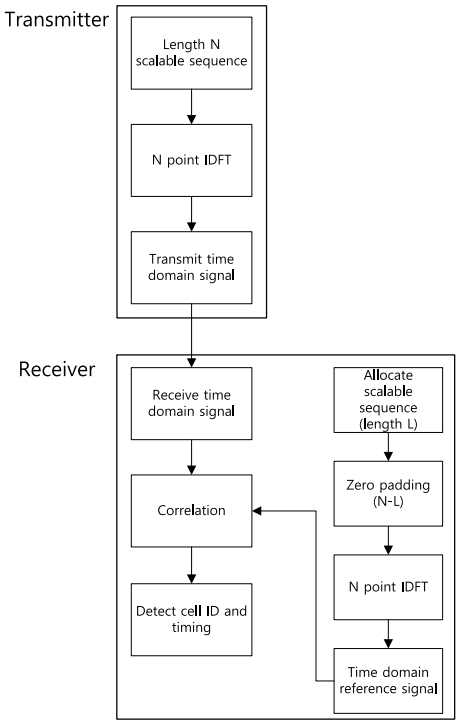

FIGURE 2. Flow chart for the scalable sequence design.

to detect the preamble. For preamble detection, the receiver generates a frequency-domain reference signal by mapping the m-sequence of length L (truncation of m-sequence with length N) and performing zero padding of dimension $(N-L)$ in the frequency domain. The time-domain reference signal is obtained by taking the N-point IDFT of its frequency-domain reference signal. The timing and cell ID are detected by correlating the received signal of length N with the time-domain reference signal of the same length N.

To check whether the M-SS has the SS property, its vector allocated to N subcarriers in the frequency domain is expressed as $\mathbf{X}_N^{MSS,c} = \left[X_0^{MSS,c} X_1^{MSS,c} \dots X_{N-1}^{MSS,c}\right]$, where c denotes the cell ID. The time-domain sequence of length N is obtained by taking IDFT of $\mathbf{X}_N^{MSS,c}$:

$$\begin{aligned}\mathbf{x}_N^{MSS,c} &= \frac{1}{N}\mathbf{X}_N^{MSS,c}\mathbf{D}^* \\ &= \left[\mathrm{x}_{N,0}^{MSS,c}\, \mathrm{x}_{N,1}^{MSS,c}\, \mathrm{x}_{N,2}^{MSS,c} \dots \mathrm{x}_{N,N-1}^{MSS,c}\right] \in \mathbf{R}^{1\times N}, \end{aligned} \quad (1)$$

where

$$\mathbf{X}_N^{MSS,c} = \left[\mathrm{X}_0^{MSS,c}\mathrm{X}_1^{MSS,c}\mathrm{X}_2^{MSS,c} \dots \mathrm{X}_{N-1}^{MSS,c}\right] \in \mathbf{R}^{1\times N}$$

$$\mathbf{D} = \begin{bmatrix} 1 & 1 & 1 & \cdots & 1 \\ 1 & \omega & \omega^2 & \cdots & \omega^{N-1} \\ 1 & \omega^2 & \omega^4 & \cdots & \omega^{2(N-1)} \\ \vdots & \vdots & \vdots & \ddots & \vdots \\ 1 & \omega^{N-1} & \omega^{2(N-1)} & \cdots & \omega^{(N-1)(N-1)} \end{bmatrix} \in \mathbf{R}^{N\times N}$$

$$\omega = e^{-j2\pi/N}.$$

The frequency-domain reference signal vector, $\mathbf{X}_L^{MSS,c}$, is obtained by mapping the m-sequence of length L and padding zeros of dimension $(N - L)$ in the frequency domain. The time-domain reference signal vector, $\mathbf{x}_L^{MSS,c} = [\mathrm{x}_{L,0}^{MSS,c}\, \mathrm{x}_{L,1}^{MSS,c} \dots \mathrm{x}_{L,N-1}^{MSS,c}]$ is obtained from IDFT of the frequency-domain reference signal. Note that the length of the time-domain reference signal is N regardless of the bandwidth corresponding to L subcarriers at the receiver. Then, the linear correlation $R_{xx}^{MSS}[m]$, between preamble $\mathbf{x}_N^{MSS,c}$ and reference signal $\mathbf{x}_L^{MSS,c}$ is expressed as follows:

If $0 < m < N$

$$\begin{aligned} R_{xx}^{MSS}[m] &= \mathbf{x}_N^{MSS,c}\left(\mathbf{S}^T\right)^m\left(\mathbf{x}_L^{MSS,c}\right)^H \\ &= \frac{1}{NL}X_N^{MSS,c}\mathbf{D}^*(\mathbf{S}^T)^m\mathbf{D}\left(\left[\mathbf{X}_L^{MSS,c}\mathbf{0}_{L-N}\right]\right)^H \\ R_{xx}^{MSS}[-m] &= \mathbf{x}_N^{MSS,c}\mathbf{S}^m(\mathbf{x}_L^{MSS,c})^H \\ &= \frac{1}{NL}\mathbf{X}_N^{MSS,c}\mathbf{D}^*\mathbf{S}^m\mathbf{D}\left(\left[\mathbf{X}_L^{MSS,c}\ \mathbf{0}_{L-N}\right]\right)^H, \end{aligned} \quad (2)$$

where

$$\mathbf{S} = \begin{bmatrix} 0 & 0 & 0 & \dots & 0 \\ 1 & 0 & 0 & \dots & 0 \\ 0 & 1 & 0 & & 0 \\ \vdots & \vdots & \vdots & \ddots & \vdots \\ 0 & 0 & \dots & 1 & 0 \end{bmatrix} \in R^{N\times N}$$

$$\mathbf{0}_N = [0\ 0\ 0\ \dots\ 0] \in R^{1\times N},$$

and

$$R_{xx}^{MSS}[0] = \frac{L}{N}.$$

The terms in (2) can also be given by

$$\begin{aligned} \left(\mathbf{D}^*(\mathbf{S}^T)^m\right)_{pq} &= \omega^{-(p-1)(q-m-1)} \in \mathbf{R}^{N\times N} \\ (\mathbf{D})_{qr} &= \omega^{(q-1)(r-1)} \in \mathbf{R}^{N\times N} \\ \left(\mathbf{D}^*(\mathbf{S}^T)^m\mathbf{D}\right)_{pr} &= \omega^{(m+1)p-(m+r)}\sum_{q=m+1}^{N}\omega^{q(r-p)} \in \mathbf{R}^{N\times N} \\ \left(\mathbf{X}\mathbf{D}^*(\mathbf{S}^T)^m\mathbf{D}\right)_{1r} &= \sum_{p=1}^{N}\sum_{q=m+1}^{N}X_{p-1}\omega^{(m+1)p-(m+r)}\omega^{q(r-p)} \\ &\quad \times \in \mathbf{R}^{1\times N}. \end{aligned} \quad (3)$$

Using (3), $R_{xx}^{MSS}[m]$, $0 < m < N$ can be expressed as

$$R_{xx}^{MSS}[m] = \frac{1}{NL}\omega^{-m}\sum_{r=1}^{N}\sum_{p=1}^{N}\left[X_{r-1}X_{p-1}\omega^{\frac{1}{2}(N+m-1)r}\omega^{-\frac{1}{2}(N-m-1)p} \cdot \frac{\sin(\pi(r-p)(N-m)/N)}{\sin(\pi(r-p)/N)}\right]. \quad (4)$$

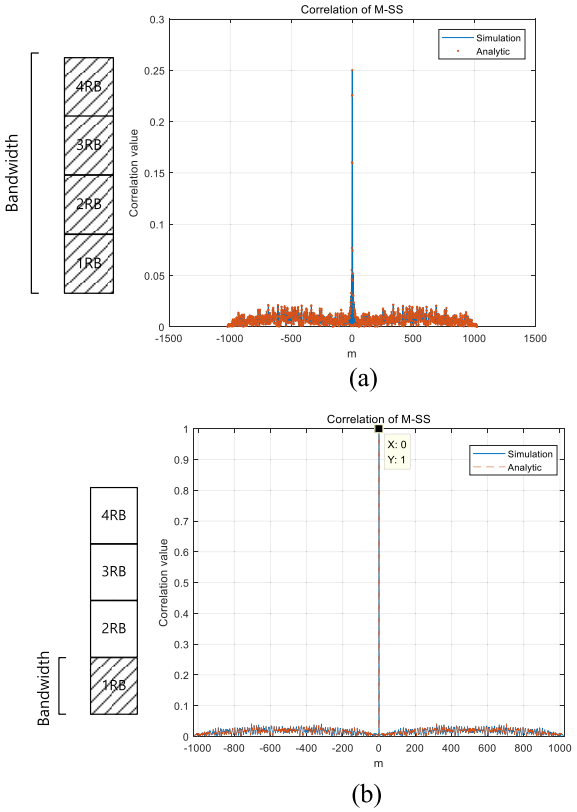

FIGURE 3. Autocorrelation property of M-SS for (a) L = N and (b) L = N/4 (RB, resource block).

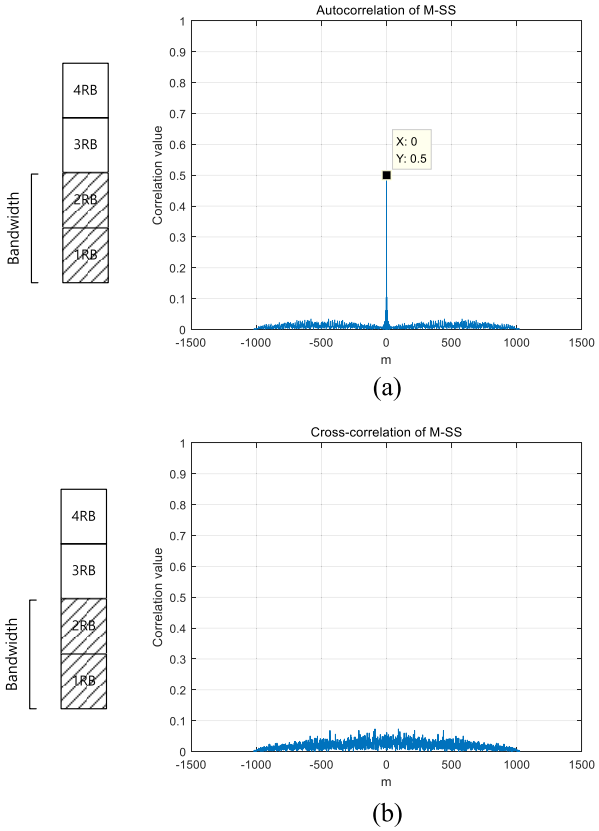

FIGURE 4. Correlation property of M-SS when L = N/2 for cell IDs (a) c =c′ and (b) c ≠c′.

Likewise, $R_{xx}^{MSS}[-m]$ and $R_{xx}^{MSS}[0]$, $0 < m < N$ can be obtained as

$$R_{xx}^{MSS}[-m] = \frac{1}{NL}\omega^{m}\sum_{r=1}^{N} \times\sum_{p=1}^{L}\left[X_{r-1}X_{p-1}\omega^{\frac{1}{2}(N-m-1)r}\omega^{-\frac{1}{2}(N+m-1)p} \cdot\frac{\sin(\pi(r-p)(N-m)/N)}{\sin(\pi(r-p)/N)}\right]$$

$$R_{xx}^{MSS}[0] = \frac{L}{N}. \quad (5)$$

From (5), it can be seen that the correlation function has maximum $R_{xx}^{MSS}[0] = \mathbf{x}\mathbf{x}^{H} = \|\mathbf{X}\|^{2}/NL = L/N$ when $m = 0$. Thus, the peak always appears at the correct timing ($m = 0$) regardless of the value of L when preamble detection is performed with M-SS.

Fig. 3 illustrates the autocorrelation property of M-SS. The cell ID used to generate the m-sequence at the transmitter is assumed to be the same as that used to generate the reference signal at the receiver. That is, the same sequence is used to generate the reference signal. Fig. 3(a) shows the case $L = N$ =1023, whereas Fig. 3(b) shows the case $L \approx N/4$, with L =256 and $N - L$ =767. The bandwidth at the receiver is marked with diagonal lines in the left-hand side graphs. The correlation obtained by (4) agrees with the simulation. In addition, the peaks occur at the correct timing and decrease with the bandwidth size.

Fig. 4 shows the correlation for the same (Fig. 4(a) for $c = c'$) and different (Fig. 4(b) for $c \neq c'$) cell IDs generating the preamble and reference signals. The signals are generated with different cyclic shifts of m-sequence in the frequency domain, corresponding to the cell IDs. We considered $L \approx N/2$ ($N = 1023$ and $L = 512$). As can be seen in these figures, the preamble is detected with the correct timing only when the same cell ID is used (Fig. 4(a)). Overall, the analyses and simulation results in this section confirm that the M-SS is an SS producing correct timing and cell IDs. The M-SS does not require any special condition on sequence length N.

IV. ZC-SS

The Zadoff–Chu (ZC) sequence is widely used for preamble design in OFDM systems because of its good correlation property and low peak-to-average power ratio (PAPR) [32]. A ZC sequence can also be converted into another ZC sequence with different root index after applying the DFT/IDFT [33]. We propose a method to generate ZC-SS for OFDM-based cellular networks. The condition for the ZC-SS to become an SS is also derived.

The ZC-SS is generated analogously to the M-SS. A ZC sequence of length N is generated at the BS and allocated to N subcarriers in the frequency domain. In the ZC-SS, the cell ID corresponding to the BS is mapped onto the root index of

the ZC sequence. The time-domain ZC sequence is obtained by the IDFT and transmitted by the BS as a preamble. At the receiver, the time-domain reference signal is obtained by applying the IDFT of the frequency-domain reference signal composed of ZC sequence of length L and zero padding of dimension $(N-L)$.

The ZC sequence is given by

$$X_N^{ZC,c}[k] = \exp\left(\frac{-j\pi ck^2}{N}\right), \quad 0 \le k < N. \tag{6}$$

The ZC sequence has the following property for length $N \ge 4$ being a power of 2:

$$\begin{aligned} X_N^{ZC,c}[k+\frac{N}{4}] &= j^k X_N^{ZC,c}[k] \\ X_N^{ZC,c}[k+\frac{2N}{4}] &= j^{2k} X_N^{ZC,c}[k] = (-1)^k X_N^{ZC,c}[k] \\ X_N^{ZC,c}[k+\frac{3N}{4}] &= j^{3k} X_N^{ZC,c}[k] = (-j)^k X_N^{ZC,c}[k], \end{aligned} \tag{7}$$

where $0 \le k < N/4$. The IDFT of the ZC sequence obtained using (7) is given by

$$\begin{aligned} & x_N^{ZC,c}[n] \\ &= \frac{1}{N}\sum_{k=0}^{N-1} X_N^{ZC,c}[k]\exp\left(\frac{j2\pi kn}{N}\right), \quad 0 \le n \le N-1 \\ &= \frac{1}{N}\sum_{k=0}^{N/4-1}\left[\begin{Bmatrix} X_N^{ZC,c}[k] \\ +X_N^{ZC,c}[k+\frac{N}{4}] \\ +X_N^{ZC,c}[k+\frac{2N}{4}] \\ +X_N^{ZC,c}[k+\frac{3N}{4}] \end{Bmatrix} \cdot \exp\left(\frac{j2\pi kn}{N}\right)\right] \\ &= \frac{1}{N}\sum_{k=0}^{N/4-1}\left[\begin{matrix} X_N^{ZC,c}[k]\left((-1)^k+1+(-j)^k+j^k\right) \\ \cdot \exp\left(\frac{j2\pi kn}{N}\right) \end{matrix}\right], \end{aligned} \tag{8}$$

where $0 \le k < N/4$. In (8), the term inside the summation, $X_N^{ZC,c}[k]\exp\left(\frac{j2\pi kn}{N}\right)\left(1+j^k+(-1)^k+(-j)^k\right)$, is non-zero when k is a multiple of four ($k = 4k'$) and zero otherwise. Hence, (8) can be rewritten as

$$\begin{aligned} x_N^{ZC,c}[n] &= \frac{4}{N}\sum_{k'=0}^{N/16-1} X_N^{ZC,c}[4k']\exp\left(\frac{j2\pi 4k'n}{N}\right) \\ &= \frac{4}{N}\sum_{k'=0}^{N/16-1}\exp\left(-\frac{j\pi c16(k')^2}{N}\right)\exp\left(\frac{j2\pi 4k'n}{N}\right) \\ &= \frac{4}{N}\exp\left(\frac{j\pi c^{-1}n^2}{N}\right) \\ &\quad \cdot \sum_{k'=0}^{N/16-1}\exp\left(\frac{-j\pi 16c(k'-\frac{1}{4}c^{-1}n)^2}{N}\right), \end{aligned} \tag{9}$$

where $0 \le k' < N/16$. Equation (9) represents the preamble in the time domain obtained from the N-point IDFT of the ZC sequence with length N. In (9), c^{-1} denotes the modular inverse of c. When $L = N/4$, the frequency-domain reference signal is obtained by allocating the ZC sequence to L sub-carriers and performing zero padding until reaching length Nin the frequency domain. When $L = N/4$, the time-domain reference signal is obtained by applying the IDFT as follows:

$$\begin{aligned} & x_L^{ZC,c}[n] \\ &= \frac{1}{4N}\sum_{k=0}^{N-1}\tilde{X}_N^{ZC,c}[k]\exp\left(\frac{j2\pi kn}{N}\right), \quad 0 \le n \le N-1, \end{aligned} \tag{10}$$

where

$$\tilde{X}_N^{ZC,c}[k] = \begin{cases} \exp\left(\frac{-j\pi ck^2}{N}\right), & 0 \le k \le \frac{N}{4}-1 \\ 0, & \frac{N}{4} \le k \le N-1. \end{cases}$$

Equation (10) can be expressed as

$$\begin{aligned} & x_L^{ZC,c}[n] \\ &= \frac{1}{4N}\sum_{k=0}^{N/4-1}\tilde{X}_N^{ZC,c}[k]\exp\left(\frac{j2\pi kn}{N}\right), \quad 0 \le n \le N-1 \\ &= \frac{1}{4N} \\ &\times\left[\begin{matrix} \sum_{k'=0}^{N/16-1}\tilde{X}_N^{ZC,c}[4k']\exp\left(\frac{j2\pi 4k'n}{N}\right) \\ +\sum_{k'=0}^{N/16-1}\left[\tilde{X}_N^{ZC,c}[4k']\exp\left(\frac{-j\pi c(8k'+1)}{N}\right)w_N^{k'}[n]p[n]\right] \\ +\sum_{k'=0}^{N/16-1}\left[\tilde{X}_N^{ZC,c}[4k']\exp\left(\frac{-j\pi c(16k'+4)}{N}\right)w_N^{k'}[n]p[2n]\right] \\ +\sum_{k'=0}^{N/16-1}\left[\tilde{X}_N^{ZC,c}[4k']\exp\left(\frac{-j\pi c(24k'+9)}{N}\right)w_N^{k'}[n]p[3n]\right] \end{matrix}\right] \\ &= \frac{1}{4N}\sum_{k'=0}^{N/16-1}\left\{\begin{matrix} \exp\left(\frac{-j\pi c(k'-\frac{1}{4}c^{-1}n)^2}{N/16}\right) \\ ++\exp\left(\frac{-j\pi c\{(k'-\frac{1}{4}(c^{-1}n-1)\}^2}{N/16}\right) \end{matrix}\right\} \\ &\quad \times\exp\left(\frac{j\pi c^{-1}n^2}{N}\right) \\ &\quad +\frac{1}{4N}\left\{\begin{matrix} +\sum_{k'=0}^{N/16-1}\exp\left(\frac{-j\pi c\{(k'-\frac{1}{4}(c^{-1}n-2)\}^2}{N/16}\right) \\ +\sum_{k'=0}^{N/16-1}\exp\left(\frac{-j\pi c\{(k'-\frac{1}{4}(c^{-1}n-3)\}^2}{N/16}\right) \end{matrix}\right\} \\ &\quad \times\exp\left(\frac{j\pi c^{-1}n^2}{N}\right), \end{aligned} \tag{11}$$

where

$$w_N^{k'}[n] = \exp\left(\frac{j2\pi 4k'n}{N}\right), \; p[n] = \exp\left(\frac{j2\pi n}{N}\right) \text{ and } 0 \le k' < N/16.$$

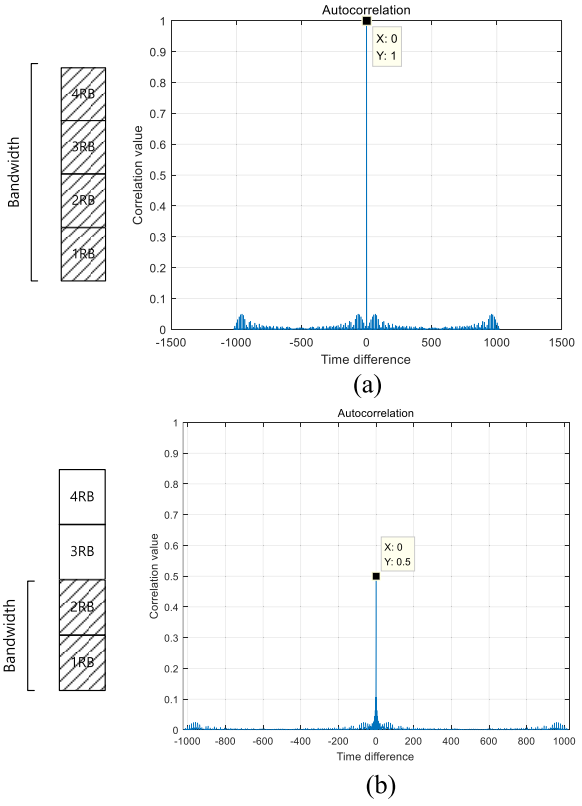

FIGURE 5. Autocorrelation property of ZC-SS for (a) L = N and (b) L = N/2 (RB, resource block).

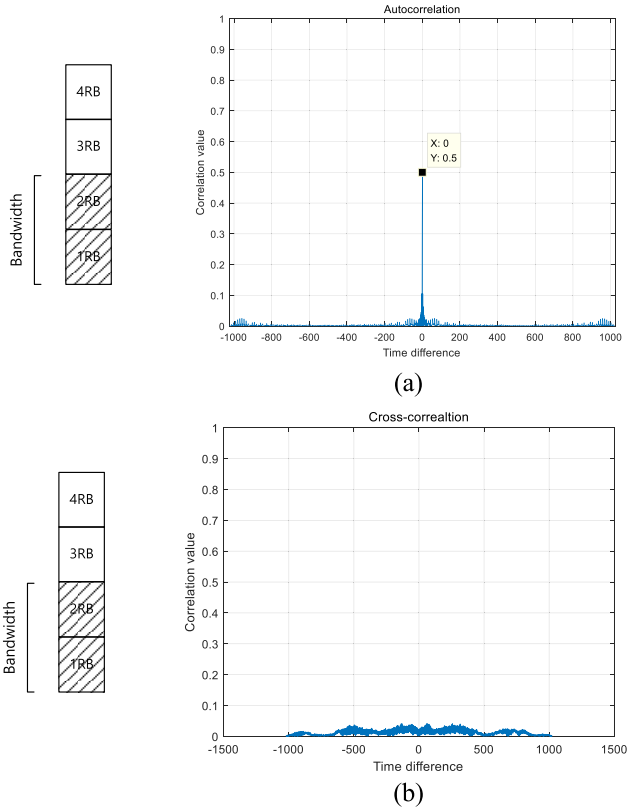

FIGURE 6. Correlation property of ZC-SS when L=N/2 for cell IDs (a) $c = c'$ and (b) $c \neq c'$.

Note that the first term of $x_L^{ZC,c}[n]$ in (11) is identical to $x_L^{ZC,c}[n]$ in (10), except for factor 1/4. As the remaining terms in (11) differ from $x_L^{ZC,c}[n]$ in (10), the cross-correlation between these two signals is low due to the pseudo-randomness of ZC sequences. At the receiver, the timing and cell ID are detected by correlating the received preamble of length N with the time-domain reference signal of the same length. As $x_N^{ZC,c}[n]$ in (9) is the time-domain synchronization signal and $x_L^{ZC,c}[n]$in (10) is the time-domain reference signal, the correlation between $x_{N/4}^{ZC,c}[n]$ and $x_N^{ZC,c'}[n]$ produces a peak value of $N/4$ when timing and cell ID agree, and a low correlation otherwise. Thus, the ZC-SS can be generated with a ZC sequence of length N if $N \geq 16$ and N is a power of 2.

Fig. 5 illustrates the autocorrelation property of ZC-SS for the same cell ID (i.e., root index) being used to generate the preamble and reference signal and $N = 1024$. Fig. 5(a) and (b) show the cases L equal to N and $N/2$, respectively. Peaks always occur at the correct timing, and the value of the peak for $L = N/2$ is half of that for $L = N$. These results confirm that the correct timing can be obtained with ZC-SS when $N \geq 16$ and N is a power of 2.

Fig. 6 shows the correlation for the same (Fig. 6(a) for $c = c'$) and different (Fig. 6(b) for $c \neq c'$) cell IDs generating the preamble and reference signal with $L = N/2$. In Fig. 6(a), the correlation between the preamble and reference signal produces a peak at the correct timing as the cell IDs agree. In contrast, Fig. 6(b) shows a low correlation as the cell IDs differ. Again, the analysis and simulation results in this section confirm that the ZC-SS is an SS producing correct timing and cell IDs if the condition on N is satisfied.

V. LFM-SS

Linear frequency modulated (LFM) signals have been widely used for surveillance applications such as radar and sonar because of their robustness to the Doppler shift [34]. Although LFM signals have also been used for preamble detection in surveillance applications, their use in cellular networks has not been reported. In cellular networks, many cell IDs should be generated and incorporated into the preamble design, such that the mobile station (MS) can distinguish among neighboring BSs. However, it is difficult to design an LFM signal carrying the transmitter identity information. We propose a method to generate LFM-SS for UAV communications over cellular networks. An LFM signal in the continuous time domain is given by

$$x_\tau(t) = e^{j\pi\left(2ft + \frac{\beta}{\tau}t^2\right)}, \tag{12}$$

where τ and β denote a symbol duration and sweeping parameter, respectively. Discretizing (12) in time results in

$$x_{N_{LFM}}^{LFM}[n] = e^{j\pi\left(2fnT + \frac{\delta n^2}{N_{LFM}}\right)}, \tag{13}$$

where $t = nT$, $T = \frac{1}{N_{LFM}\,\Delta f}$.

Here, T, Δf, and N_{LFM} denote the sampling period, subcarrier spacing, and number of samples in the LFM signal, respectively. Also, δ denotes product $\beta \cdot T$. For a given δ, we can generate only two different LFM signals of up-chirp and down-chirp types. In the proposed LFM-SS, different cell IDs are generated by combining the up-chirp and down-chirp signals for fixed δ in different patterns. Fig. 7 illustrates LFM-SS comprising a sequence of up-chirp, up-chirp, down-chirp, and up-chirp signals, representing one of the 16 possible cell IDs. In this example, the sequence length of an LFM-SS is given by $N = 4N_{LFM}$.

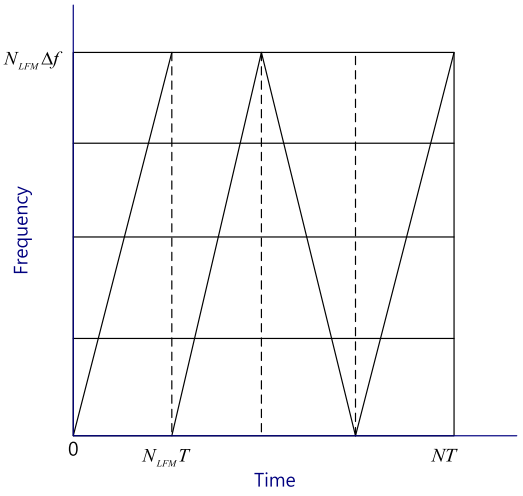

FIGURE 7. Example of LFM-SS for $N = 4N_{LFM}$.

At the receiver, different patterns of LFM signals with the same δ are generated as reference signals and correlated with the received preamble. The timing and cell ID are detected using serial or parallel correlators with the reference signals. The cell ID is detected when the patterns of the received signal and reference signal match. However, in the LFM-SS, the UAV receives signals with bandwidth according to the channel condition. As the bandwidth is proportional to the symbol duration in the LFM case for a given δ, the length L of the reference signal in LFM-SS changes depending on the channel condition. For example, L is set to N_{LFM} when the UAV receives the signal with full bandwidth and to $N_{LFM}/4$ when the UAV receives the signal with a quarter of the bandwidth.

Next, the correlation between the preamble with full bandwidth and reference signal with different bandwidth is analyzed to check the scalable property of LFM-SS. Here, $x^{LFM}_{N_{LFM}}[n]$ represents the preamble of length N_{LFM} at the transmitter, and $x^{LFM}_{L}[n]$ represents the reference signal of length L at the receiver. When $L = N_{LFM}$, the correlation between the preamble and reference signal is given by

$$R^{LFM}_{xx}[m] = \sum_{n=-\infty}^{\infty} x^{LFM}_{N_{LFM}}[n] x^{LFM^*}_{N_{LFM}}[n-m]. \tag{14}$$

The correlation results for $m \geq 0$ and $m < 0$ are given by

$$\begin{aligned} R^{LFM}_{xx}[m] &= \exp\left(\frac{-j\pi\delta m^2}{N_{LFM}}\right) \sum_{m=n}^{N} \exp\left(\frac{j2\pi\delta mn}{N_{LFM}}\right), \quad m \geq 0 \\ \left|R^{LFM}_{xx}[m]\right| &= \left|\frac{\sin(\pi\delta m(N_{LFM} - m + 1)/N_{LFM})}{\sin(\pi\delta m/N_{LFM})}\right|, \quad m \geq 0 \end{aligned} \tag{15}$$

$$\begin{aligned} R^{LFM}_{xx}[m] &= \exp\left(\frac{-j\pi\delta m^2}{N_{LFM}}\right) \sum_{r=0}^{N+n} \exp\left(\frac{j2\pi\delta mn}{N_{LFM}}\right), \quad m < 0 \\ \left|R^{LFM}_{xx}[m]\right| &= \left|\frac{\sin(\pi\delta m(N_{LFM} + m + 1)/N_{LFM})}{\sin(\pi\delta m/N_{LFM})}\right|, \quad m < 0 \end{aligned} \tag{16}$$

When $m = 0$, the maximum of $\left|R^{LFM}_{xx}[m]\right| = N_{LFM}$ is obtained. Fig. 8 compares the analytic results in (15) and (16) with the simulation results when $N_{LFM} = 1024$. The simulation results agree well with the analytic results. Timing is correctly detected when the reference signal with $L = N_{LFM}$ is used.

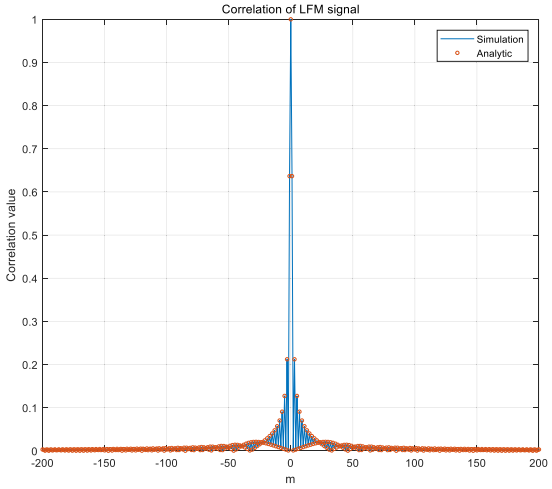

FIGURE 8. Correlation of LFM signal when $L = N_{LFM}$.

The scalable property of LFM-SS can be analyzed by correlating the preamble of length N_{LFM} with the reference signal of different length L. When$L = N_{LFM}/4$, the correlation between the preamble and reference signal is given by

$$\begin{aligned} R^{LFM}_{xx}[m] &= \sum_{n=-\infty}^{\infty} x^{LFM}_{N_{LFy}}[n] x^{IFM^*}_{L}[n-m] \\ &= \exp\left(\frac{-j\pi\delta m^2}{N_{LFM}}\right) \\ &\quad \cdot \sum_{n=-\infty}^{\infty} \left[\begin{array}{l} rect\left(\frac{n}{N_{LFM}} - \frac{1}{2}\right) rect\left(\frac{n-m}{N_{LFM}/4} - \frac{1}{2}\right) \\ \cdot \exp\left(\frac{j2\pi\delta mn}{N_{LFM}}\right) \end{array} \right]. \end{aligned} \tag{17}$$

The correlation results for three different regions of m can be obtained as follows.

If $-\frac{N_{LFM}}{4} \le m < 0$,

$$R_{xx}^{LFM}[m] = \exp\left(\frac{-j\pi\delta m^2}{N_{LFM}}\right)\sum_{n=0}^{m-1+N_{LFM}/4}\exp\left(\frac{j2\pi\delta mn}{N_{LFM}}\right)$$
$$= \exp\left(\frac{-j\pi\delta m^2}{N_{LFM}}\right)\frac{\sin(\pi\delta m(m+N_{LFM}/4))}{\sin(\pi\delta m/N_{LFM})}$$
$$\left|R_{xx}^{LFM}[m]\right| = \left|\frac{\sin(\pi\delta m(m+N_{LFM}/4))}{\sin(\pi\delta m/N_{LFM})}\right|. \quad (18)$$

If $0 \le m < \frac{3}{4}N_{LFM}$,

$$R_{xx}^{LFM}[m] = \exp\left(\frac{-j\pi\delta m^2}{N_{LFM}}\right)\sum_{n=m}^{N_{LFM}/4+m-1}\exp\left(\frac{j2\pi\delta mn}{N_{LFM}}\right)$$
$$= \exp\left(\frac{-j\pi\delta m(m+N_{LFM}/4)}{N_{LFM}}\right)\frac{\sin(\pi\delta m/4)}{\sin(\pi\delta m/N_{LFM})}$$
$$\left|R_{xx}^{LFM}[m]\right| = \left|\frac{\sin(\pi\delta m/4)}{\sin(\pi\delta m/N_{LFM})}\right|. \quad (19)$$

If $\frac{3}{4}N_{LFM} \le m < N_{LFM}$,

$$R_{xx}^{LFM}[m] = \exp\left(\frac{-j\pi\delta m^2}{N_{LFM}}\right)\sum_{n=m}^{N_{LFM}-1}\exp\left(\frac{j2\pi\delta mn}{N_{LFM}}\right)$$
$$= \exp\left(\frac{j\pi\delta m^2}{N_{LFM}}\right)\frac{\sin(\pi\delta m(N_{LFM}-m)/N_{LFM})}{\sin(\pi\delta m/N_{LFM})}$$
$$\left|R_{xx}^{LFM}[m]\right| = \left|\frac{\sin(\pi\delta m(N_{LFM}-m)/N_{LFM})}{\sin(\pi\delta m/N_{LFM})}\right|. \quad (20)$$

Fig. 9 compares the analytic results in (18), (19), and (20) with the simulation results when $N_{LFM} = 1024$. Correct timing can be also detected for the reference signal with $L = N_{LFM}/4$. Again, the simulation results agree well with the analytic results.

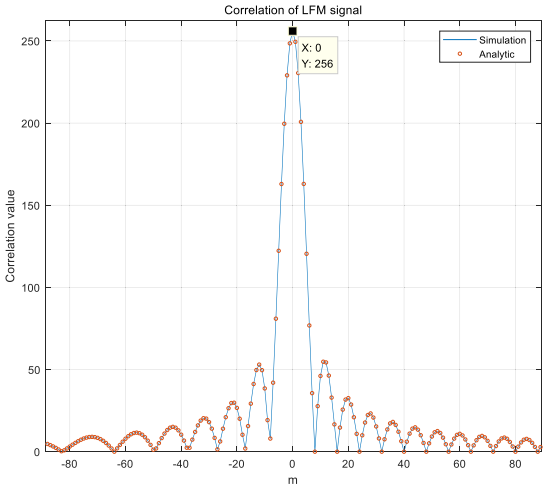

FIGURE 9. Correlation of LFM signal when $L = N_{LFM}/4$.

Next, we examine the autocorrelation property of an LFM signal under Doppler shift, because a substantial shift may occur in UAV cellular networks due to the rapid motion of the vehicle. The autocorrelation of the LFM signal of length N_{LFM} in Doppler environments can be expresses as

$$R_{xx}^{LFM}[m] = \sum_{n=-\infty}^{\infty} x_{N_{LFM}}^{LFM}[n]x_{N_{LFM}}^{LFM^*}[n-m]e^{\frac{j2\pi\varepsilon n}{N_{LFM}}}, \quad (21)$$

where ε denotes a normalized carrier frequency offset. The correlation results from (19) for $m \ge 0$ and $m < 0$ are given as follows. If $m \ge 0$,

$$R_{xx}^{LFM}[m] = \exp(j\pi\varepsilon(1+\frac{m}{N_{LFM}}))\exp(j\pi\delta m)$$
$$\cdot\frac{\sin(\pi(\delta m+\varepsilon)(N_{LFM}-m+1)/N_{LFM})}{\sin(\pi(\delta m+\varepsilon)/N_{LFM})}$$
$$\left|R_{xx}^{LFM}[m]\right| = \left|\frac{\sin(\pi(\delta m+\varepsilon)(N_{LFM}-m+1)/N_{LFM})}{\sin(\pi(\delta m+\varepsilon)/N_{LFM})}\right|. \quad (22)$$

If $m < 0$,

$$R_{xx}^{LFM}[m] = \exp(j\pi\varepsilon(1+\frac{m}{N_{LFM}}))\exp(j\pi\delta m)$$
$$\cdot\frac{\sin(\pi(\delta m+\varepsilon)(N_{LFM}+m+1)/N_{LFM})}{\sin(\pi(\delta m+\varepsilon)/N_{LFM})}$$
$$\left|R_{xx}^{LFM}[m]\right| = \left|\frac{\sin(\pi(\delta m+\varepsilon)(N_{LFM}+m+1)/N_{LFM})}{\sin(\pi(\delta m+\varepsilon)/N_{LFM})}\right|. \quad (23)$$

Fig. 10 compares the analytic results in (22) and (23) with the simulation results for varying ε. Here, only the maximum correlation values for ε are plotted. The simulation results agree with the analytic results. The preamble can be detected even under a high Doppler shift because the maximum correlation is larger than 0.9 for everyε. Here, the analysis is performed on one LFM signal of length N_{LFM} for notational convenience. Similar results are obtained for LFM-SS of length N with different patterns.

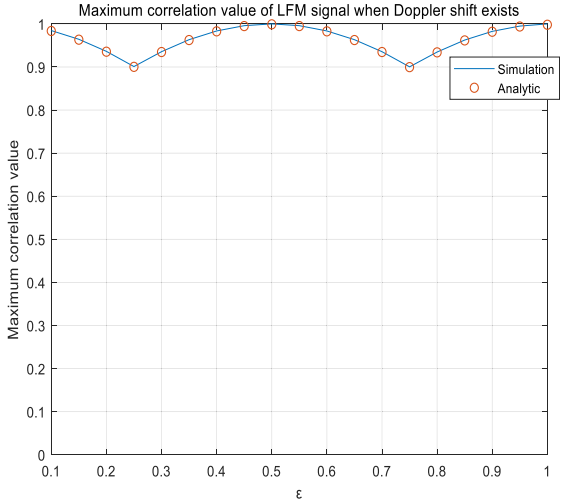

FIGURE 10. Maximum correlation of LFM signal under Doppler shift.

VI. SIMULATIONS

We evaluated the performance of the three proposed SSs for UAV communications over cellular networks. First, we evaluated the effect of Doppler shifts when the SSs are used for

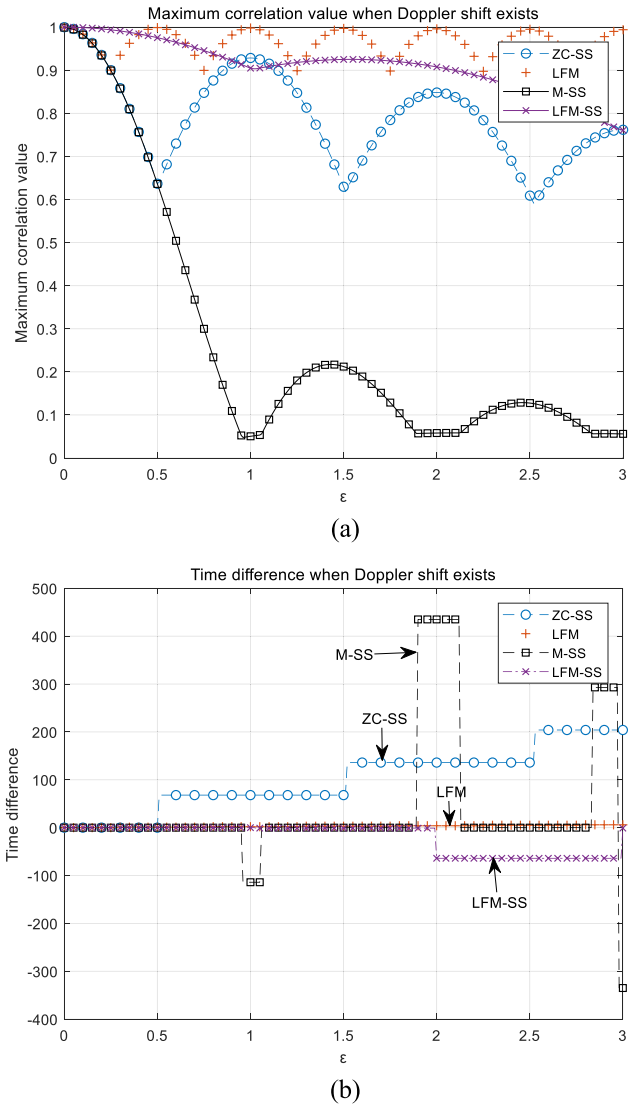

FIGURE 11. Performance of SSs under Doppler shift: (a) maximum correlation and (b) time difference.

preamble in OFDM-based UAV cellular networks. Fig. 11 shows the maximum correlation values of the three SSs for varying ε. Here, the result of the LFM signal in Fig. 10 is inserted for comparison. In Fig. 11, the maximum correlation of the LFM signal is above 0.9 for every ε. Hence, the preamble based on the LFM can provide the best performance in Doppler environments. However, the LFM signal cannot be used for SS design in UAV cellular networks because it can provide only two cell IDs (up-chirp and down-chirp). Among the proposed SSs, the LFM-SS shows the best performance (slightly worse than the LFM signal, but better than ZC-SS and M-SS) because this SS is generated using the LFM signal. Fig. 11(b) shows the difference between the real and estimated timing instants under Doppler shift. The timing was estimated as the instant when maximum correlation occurred. Among the three SSs (excluding the LFM signal), the LFM-SS shows the best performance (smallest timing error).

Fig. 12 shows the detection probability of the three proposed SSs at the receiver when no Doppler shift exists. Here, a successful detection corresponds to the case where the correct timing and cell ID are detected. We compared the SS performance for two lengths, L, of N and $N/4$. The detection probability of the three SSs with full bandwidth ($L = N$) at the receiver is almost the same. In addition, the transmitted preamble can be correctly detected under low signal-to-noise ratio (SNR) even with a quarter of the bandwidth (i.e., $L = N/4$). As SSs with a quarter of the bandwidth are used under a good channel condition, the performance loss caused by this bandwidth in Fig. 12 can be compensated by a small pathloss (good channel) in the proposed technique. In this case, UAV battery power is saved by the narrow bandwidth. On the other hand, the performance gain obtained by SSs with a full bandwidth will be offset by a large pathloss (poor channel) in the proposed technique. In this case, a weak signal received at the UAV can be compensated by the gain in Fig. 12.

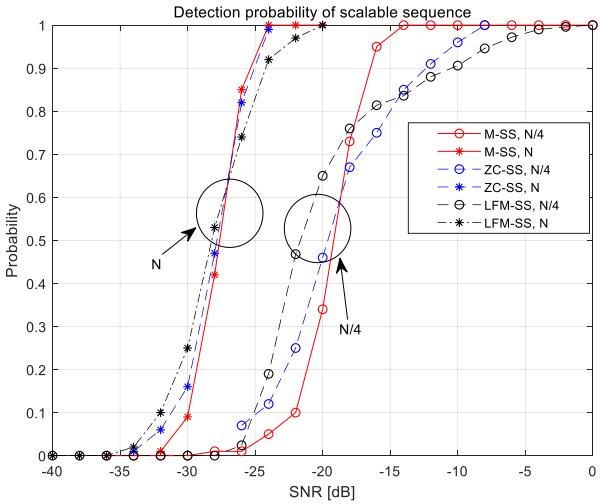

FIGURE 12. Detection probabilities of SSs for varying length L.

Fig. 13 shows the detection probability of the three SSs under Doppler shift ($\varepsilon = 0, 0.5, 1$). Simulation is performed using the 3D spatial channel model (SCM). A Rician fading channel with a K-factor of 25 dB is employed for simulation [35]–[40]. The Rician fading channel is composed of an LoS path and a non-LoS path consisting of 20 rays. In simulation, it is assumed that the height of UAV is 70 meter above from ground, height of BS is 30 meter, and UAV is 51 meter away from BS. The detection probability is similar among SSs when $\varepsilon = 0$. When $\varepsilon = 1$, the performance degradation of the LFM-SS is negligible. However, the detection probability of M-SS and ZC-SS substantially decreases under Doppler shift and converges to 0. As can be expected from the results in Fig. 11, the LFM-SS provides the highest detection probability in Doppler environments.

The properties of the proposed three sequences are summarized in Table 1. It is preferable to use M-SS and ZC-SS when Doppler shift is small, because their sensitivity to Doppler

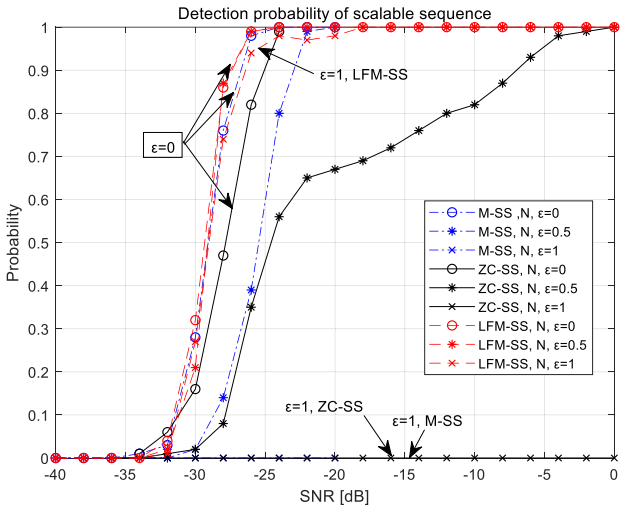

FIGURE 13. Detection probability of SS under Doppler shift.

TABLE 1. Properties of three scalable sequences.

Sequence	Doppler sensitivity	Limit on SS length	Cell-ID mapping
M-SS	Very weak	No limitation	Cyclic shift
ZC-SS	Weak	SS length N ≥ 16 and N is a power of 2	Root index
LFM-SS	Robust to Doppler	No limitation	Up-chirp and down-chirp pattern

shift. When ZZ-SS is used, the conditions on the length of ZZ-SS should be satisfied. When Doppler shift is high, it will be beneficial to use LFM-SS because its insensitivity to Doppler shift.

VII. CONCLUSION

We propose a preamble design technique for UAV communications over cellular networks to efficiently use the battery capacity of UAVs. We show that the three proposed SSs enable the UAV to correctly detect the timing and cell ID with bandwidth depending on the channel condition. The M-SS provides the highest detection probability with no Doppler shift. However, its performance substantially decreases with Doppler shift. Hence, the M-SS may be preferable in cellular networks with carrier frequency below 6 GHz, where the Doppler effect is not significant. Similar performance can be obtained for the ZC-SS if the condition on the sequence length is satisfied. Furthermore, for LFM-SS, a negligible degradation of performance (i.e., detection probability) occurs even under high Doppler shift, because the LFM-SS is based on the Doppler-insensitive LFM signals. Thus, the LFM-SS may be preferable in UAV cellular networks with carrier frequency above 6 GHz, where the Doppler effect must be considered.

REFERENCES

[1] H. Baek and J. Lim, "Design of future UAV-relay tactical data link for reliable UAV control and situational awareness," *IEEE Commun. Mag.*, vol. 56, no. 10, pp. 144–150, Oct. 2018.

[2] K. Kuru, D. Ansell, W. Khan, and H. Yetgin, "Analysis and optimization of unmanned aerial vehicle swarms in logistics: An intelligent delivery platform," *IEEE Access*, vol. 7, pp. 15804–15831, 2019.

[3] Y. Zeng, J. Lyu, and R. Zhang, "Cellular-connected UAV: Potential, challenges, and promising technologies," *IEEE Wireless Commun.*, vol. 26, no. 1, pp. 120–127, Feb. 2019.

[4] H. Wang, J. Wang, J. Chen, Y. Gong, and G. Ding, "Network-connected UAV communications: Potentials and challenges," *China Commun.*, vol. 15, no. 12, pp. 111–121, Dec. 2018.

[5] L. Gupta, R. Jain, and G. Vaszkun, "Survey of important issues in UAV communication networks," *IEEE Commun. Surveys Tuts.*, vol. 18, no. 2, pp. 1123–1152, 2nd Quart., 2016.

[6] H. Zhao, H. Wang, W. Wu, and J. Wei, "Deployment algorithms for UAV airborne networks toward on-demand coverage," *IEEE J. Sel. Areas Commun.*, vol. 36, no. 9, pp. 2015–2031, Sep. 2018.

[7] A. A. Alkheir, M. Aloqaily, and H. T. Mouftah, "Connected and autonomous electric vehicles (CAEVs)," *IT Prof.*, vol. 20, no. 6, pp. 54–61, Nov./Dec. 2018.

[8] H. Ullah, N. G. Nair, A. Moore, C. Nugent, P. Muschamp, and M. Cuevas, "5G communication: An overview of vehicle-to-everything, drones, and healthcare use-cases," *IEEE Access*, vol. 7, pp. 37251–37268, 2019.

[9] *Technical Specification Group Radio Access Network; Study on Enhanced LTE Support for Aerial Vehicles (Release 15) V15.0.0*, document TR 36.777, 3GPP, 2017.

[10] *Potential Enhancements for UAV Interference Problem*, document Tdoc R2-1705426, TSG-RAN WG#2, 2017.

[11] L. Liu, S. Zhang, and R. Zhang, "Multi-Beam UAV communication in cellular uplink: Cooperative interference cancellation and sum-rate maximization," 2018, *arXiv:1808.00189*. [Online]. Available: https://arxiv.org/abs/1808.00189

[12] G. Geraci, A. G. Rodriguez, L. G. Giordano, D. L. Pérez, and E. Björnson, "Understanding UAV cellular communications: From existing networks to massive MIMO," *IEEE Access*, vol. 6, pp. 67853–67865, 2018.

[13] V. Yajnanarayana, Y.-P. E. Wang, S. Gao, S. Muruganathan, and X. L. Ericsson, "Interference mitigation methods for unmanned aerial vehicles served by cellular networks," in *Proc. IEEE 5G World Forum (5GWF)*, Silicon Valley, CA, USA, Jul. 2018, pp. 118–122.

[14] W. Zhong, L. Xu, Q. Zhu, X. Chen, and J. Zhou, "MmWave beamforming for UAV communications with unstable beam pointing," *China Commun.*, vol. 16, no. 1, pp. 37–46, Jan. 2019.

[15] L. Zhu, J. Zhang, Z. Xiao, X. Cao, D. O. Wu, and X.-G. Xia, "3-D beamforming for flexible coverage in millimeter-wave UAV communications," *IEEE Wireless Commun. Lett.*, vol. 8, no. 3, pp. 837–840, Jun. 2019.

[16] Q. Yuan, Y. Hu, C. Wang, and Y. Li, "Joint 3D beamforming and trajectory design for UAV-enabled mobile relaying system," *IEEE Access*, vol. 7, pp. 26488–26496, 2019.

[17] S. J. Maeng, H.-I. Park, and Y. S. Cho, "Preamble design technique for GMSK-based beamforming system with multiple unmanned aircraft vehicles," *IEEE Trans. Veh. Technol.*, vol. 66, no. 8, pp. 7098–7113, Aug. 2017.

[18] L. Yang and W. Zhang, "Hierarchical codebook and beam alignment for UAV communications," in *Proc. IEEE Globecom Workshops (GC Wkshps)*, Abu Dhabi, UAE, Dec. 2018, pp. 1–6.

[19] J. Zhao and W. Jia, "Efficient channel tracking strategy for mmWave UAV communications," *Electron. Lett.*, vol. 54, no. 21, pp. 1218–1220, Oct. 2018.

[20] X. Lin, V. Yajnanarayana, S. D. Muruganathan, S. Gao, H. Asplund, H.-L. Maattanen, M. Bergstrom, S. Euler, and Y.-P. E. Wang, "The sky is not the limit: LTE for unmanned aerial vehicles," *IEEE Commun. Mag.*, vol. 56, no. 4, pp. 204–210, Apr. 2018.

[21] A. Al-Hourani and K. Gomez, "Modeling cellular-to-UAV path-loss for suburban environments," *IEEE Wireless Commun. Lett.*, vol. 7, no. 1, pp. 82–85, Feb. 2018.

[22] R. Amorim, H. Nguyen, P. Mogensen, I. Z. Kovács, J. Wigard, and T. B. Sørensen, "Radio channel modeling for UAV communication over cellular networks," *IEEE Wireless Commun. Lett.*, vol. 6, no. 4, pp. 514–517, Aug. 2017.

[23] B. Galkin, J. Kibilda, and L. A. DaSilva, "UAVs as mobile infrastructure: Addressing battery lifetime," *IEEE Commun. Mag.*, vol. 57, no. 6, pp. 132–137, Jun. 2019.
[24] M. Y. Selim and A. E. Kamal, "Post-disaster 4G/5G network rehabilitation using drones: Solving battery and backhaul issues," in *Proc. IEEE Globecom Workshops (GC Wkshps)*, Abu Dhabi, UAE, Dec. 2018, pp. 1–6.
[25] Z. Zhou, J. Feng, B. Gu, B. Ai, S. Mumtaz, J. Rodriguez, and M. Guizani, "When mobile crowd sensing meets UAV: Energy-efficient task assignment and route planning," *IEEE Trans. Commun.*, vol. 66, no. 11, pp. 5526–5538, Nov. 2018.
[26] H. Jian and Z. Yue-tong, "Impact of Doppler on high speed UAV OFDM system," in *Proc. Int. Conf. Commun. Softw. Netw.*, Macau, China, pp. 742–745, Feb. 2009.
[27] V. Vahidi and E. Saberinia, "Orthogonal frequency division multiplexing and channel models for payload communications of unmanned aerial systems," in *Proc. Int. Conf. Unmanned Aircraft Syst. (ICUAS)*, Arlington, VA, USA, Jun. 2016, pp. 1156–1161.
[28] Y. Zeng, J. Xu, and R. Zhang, "Energy minimization for wireless communication with rotary-wing UAV," *IEEE Trans. Wireless Commun.*, vol. 18, no. 4, pp. 2329–2345, Apr. 2019.
[29] B. Uragun, "Energy efficiency for unmanned aerial vehicles," in *Proc. 10th Int. Conf. Mach. Learn. Appl. Workshops*, Honolulu, HI, USA, Dec. 2011, pp. 316–320.
[30] *Evolved Universal Terrestrial Radio Access (E-UTRA) and Evolved Universal Terrestrial Radio Access Network (E-UTRAN); Physical Channels and Modulation, v. 13.3.0*, document TS36.211, 3GPP, Sep. 2016.
[31] *5G; NR; Physical Channels and Modulation, v. 15.2.0*, document TS38.211, 3GPP, Jul. 2018.
[32] R. Frank, "Polyphase codes with good nonperiodic correlation properties," *IEEE Trans. Inf. Theory*, vol. IT-9, no. 1, pp. 43–45, Jan. 1963.
[33] S. Beyme and C. Leung, "Efficient computation of DFT of Zadoff-Chu sequences," *Electron. Lett.*, vol. 45, no. 9, pp. 461–463, Apr. 2009.
[34] M. A. Richards, *Fundamentals of Radar Signal Processing*. New York, NY, USA: McGraw-Hill, 2005.
[35] M. Mozaffari, W. Saad, M. Bennis, Y.-H. Nam, and M. Debbah, "A tutorial on UAVs for wireless networks: Applications, challenges, and open problems," *IEEE Commun. Surveys Tuts.*, to be published. doi: 10.1109/COMST.2019.2902862.
[36] D. W. Matolak and R. Sun, "Air-ground channel characterization for unmanned aircraft systems: The hilly suburban environment," in *Proc. IEEE 80th Veh. Technol. Conf. (VTC2014-Fall)*, Vancouver, BC, Canada, Sep. 2014, pp. 1–5.
[37] R. Sun and D. W. Matolak, "Air–ground channel characterization for unmanned aircraft systems part II: Hilly and mountainous settings," *IEEE Trans. Veh. Technol.*, vol. 66, no. 3, pp. 1913–1925, Mar. 2017.
[38] D. W. Matolak and R. Sun, "Initial results for air-ground channel measurements & modeling for unmanned aircraft systems: Over-sea," in *Proc. IEEE Aerosp. Conf.*, Big Sky, MT, USA, Mar. 2014, pp. 1–15.
[39] D. W. Matolak and R. Sun, "Air-ground channel characterization for unmanned aircraft systems: The near-urban environment," in *Proc. IEEE Mil. Commun. Conf. (MILCOM)*, Tampa, FL, USA, Oct. 2015, pp. 1656–1660.
[40] Q. Zhu, K. Jiang, X. Chen, W. Zhong, and Y. Yang, "A novel 3D non-stationary UAV-MIMO channel model and its statistical properties," *China Commun.*, vol. 15, no. 12, pp. 147–158, Dec. 2018.

SU HYUK MOON was born in Daejeon, South Korea, in 1992. He received the B.S. and M.S. degrees in electrical and electronics engineering from Chung-Ang University, Seoul, South Korea, in 2015, 2018 respectively, where he is currently pursuing the Ph.D. degree in electrical and electronics engineering and has been a Research Assistant with the Mobile Communications Lab, since 2016. His research interests include wireless communication systems and digital signal processing.

CHANG HWAN PARK was born in Busan, South Korea, in 1982. He received the B.S., M.S., and Ph.D. degrees in electrical and electronics engineering from Chung-Ang University, Seoul, South Korea, in 2005, 2007, and 2011, respectively.

From 2005 to 2011, he was a Research Assistant with the Mobile Communications Lab, Chung-Ang University. Since 2011, he has been a Deputy Principle Research Engineer with LG Electronics, Seoul. He has been involved in standardization activities of LTE and 5G NR in 3GPP and developing a Multi-MODEM chipset for HSPA+, LTE-A, and 5G. He has authored more than 50 conferences and articles. His research interests include mobile communication and digital signal processing, especially for MIMO-OFDM and 5G.

YONG SOO CHO was born in South Korea. He received the B.S. degree in electronics engineering from Chung-Ang University, Seoul, South Korea, in 1984, the M.S. degree in electronics engineering from Yonsei University, Seoul, in 1987, and the Ph.D. degree in electrical and computer engineering from The University of Texas, Austin, TX, USA, in 1991.

In 1984, he was a Research Engineer with Goldstar (LG) Electrical Company, Osan, South Korea. In 2001, he was a Visiting Research Fellow with the Electronics and Telecommunications Research Institute (ETRI). Since 1992, he has been a Professor with the School of Electrical and Electronics Engineering, Chung-Ang University. He has authored 12 books, more than 400 conference and articles, and more than 120 patents. His research interests include mobile communication and digital signal processing, especially for MIMO OFDM and 5G. He served as a recipient of the Dr. Irwin Jacobs Award, in 2013. He was served as the President for the Korean Institute of Communications and Information Sciences, in 2016.